Digital Signal Processing 130 (2022) 103695

Contents lists available at ScienceDirect

Digital Signal Processing

www.elsevier.com/locate/dsp

Filterable sample consensus based on angle variance for pupil segmentation

Jitao Zhong [a], Dixin Wang [a], Hongtong Wu [a], Peng Wang [c], Minqiang Yang [a,*], Hong Peng [a,b,**], Bin Hu [a,d,e,**]

[a] Gansu Provincial Key Laboratory of Wearable Computing, School of Information Science and Engineering, Lanzhou University, Lanzhou 730000, China
[b] Key Laboratory of Special Functional Materials and Structural Design, Ministry of Education, Lanzhou University, Lanzhou 730000, China
[c] School of Mathematics and Statistics, Huazhong University of Science and Technology, Wuhan 430074, China
[d] Brain Health Engineering Lab, School of Medical Technology, Beijing Institute of Technology, Beijing 100081, China
[e] CAS Center for Excellence in Brain Science and Intelligence Technology, Shanghai Institutes for Biological Sciences, Chinese Academy of Sciences, Shanghai 200031, China

ARTICLE INFO

Article history:
Available online 22 August 2022

Keywords:
Angle variance factor
Sample consensus
Boundary locator
Pupil segmentation

ABSTRACT

Pupil segmentation is a first and important topic of iris recognition, identity recognition and eye movement information extraction for mental analysis. However, due to the negative effects of eyelash occlusion, eyelid occlusion and off-gaze deflection, making a precise pupil segmentation is a difficult task. Therefore, we propose a precise and robust algorithm for pupil segmentation, namely Angle Variance based Filterable Sample Consensus (AVBFSC), which is composed of an outlier filter and a boundary locator. The outlier filter can eliminate negative effects mentioned above, and also a best pupil segmentation is performed with our boundary locator, which learns a circular mathematical equation by selecting sub-samples from pupil edge pixels randomly. Experiment results in comparison with state-of-the-art methods on CASIA-Iris-V4-Interval dataset, indicate that our algorithm achieved best performance, that is, Accuracy of 98.99%, False Acceptance Rate (FAR) of 2.09% and Genuine Acceptance Rate (GAR) of 98.54%. In addition, it also has robust results under the condition of specific non-ideal scenes from CASIA-Iris-V4-Lamp dataset and Indian Institute of Technology Delhi (IITD) dataset including dark light conditions, eyelash occlusion, eyelid occlusion and off-gaze deflection.

1. Introduction

Bio-information, face emotion, iris, pupil, fingerprints and gait [1–3], are the important information to recognizing human identity [4–7]. Further, it's crucial for pupil image to establish iris recognition system [8,9], analyze depression characteristics, study the attention of students by locating pupil and performing gaze tracking. Thus, pupil segmentation is the first and essential step for achieving above researches. Belcher et al. [10] report that pupil is nearly circular region and its size can change timely depending on the amount of light entering eyes. So, some circular-edge based segmentation techniques are commonly raised. It's also reported that the changes of pupil's size can reflect the affective fluctuation of a mentally handicapped [11], such as depression patients, patients with autism and anxiety sufferers, under the stimuli of different emotional scenes. Nowadays, existing pupil segmentation technologies have achieved pretty good results from ideal iris image but not from a lot of specific non-ideal scenes including dark light conditions, eyelash occlusion, eyelid occlusion and off-gaze deflection. In our work, the main focus is to perform a precise and robust pupil segmentation in both ideal and non-ideal scenes.

Daugman [12] proposes the integro-differential operator (IDO) to find both outer and inner boundaries (i.e. pupil boundary) of a given iris image. A soft-computing approach [13] is used for the segmentation of pupil and iris localization based on rough entropy and circular sector analysis, and has an accuracy of 97.12% in an ideal iris dataset but not in specific non-ideal scenes. Circular hough transform (CHT) is proposed by Wildes [14] to search for the most possible iris boundary by using edge point voting technology. Weighted adaptive hough and ellipsopolar transforms (WAHET) [15], proposed by Uhl and Wild, naturally complements the previous CHT in theory, but still performs not pretty good in specific non-ideal scenes as the same as CHT. In this paper, AVBFSC

* Corresponding author.
** Corresponding authors at: Gansu Provincial Key Laboratory of Wearable Computing, School of Information Science and Engineering, Lanzhou University, Lanzhou 730000, China.
E-mail addresses: yangmq@lzu.edu.cn (M. Yang), pengh@lzu.edu.cn (H. Peng), bh@lzu.edu.cn (B. Hu).

https://doi.org/10.1016/j.dsp.2022.103695
1051-2004/

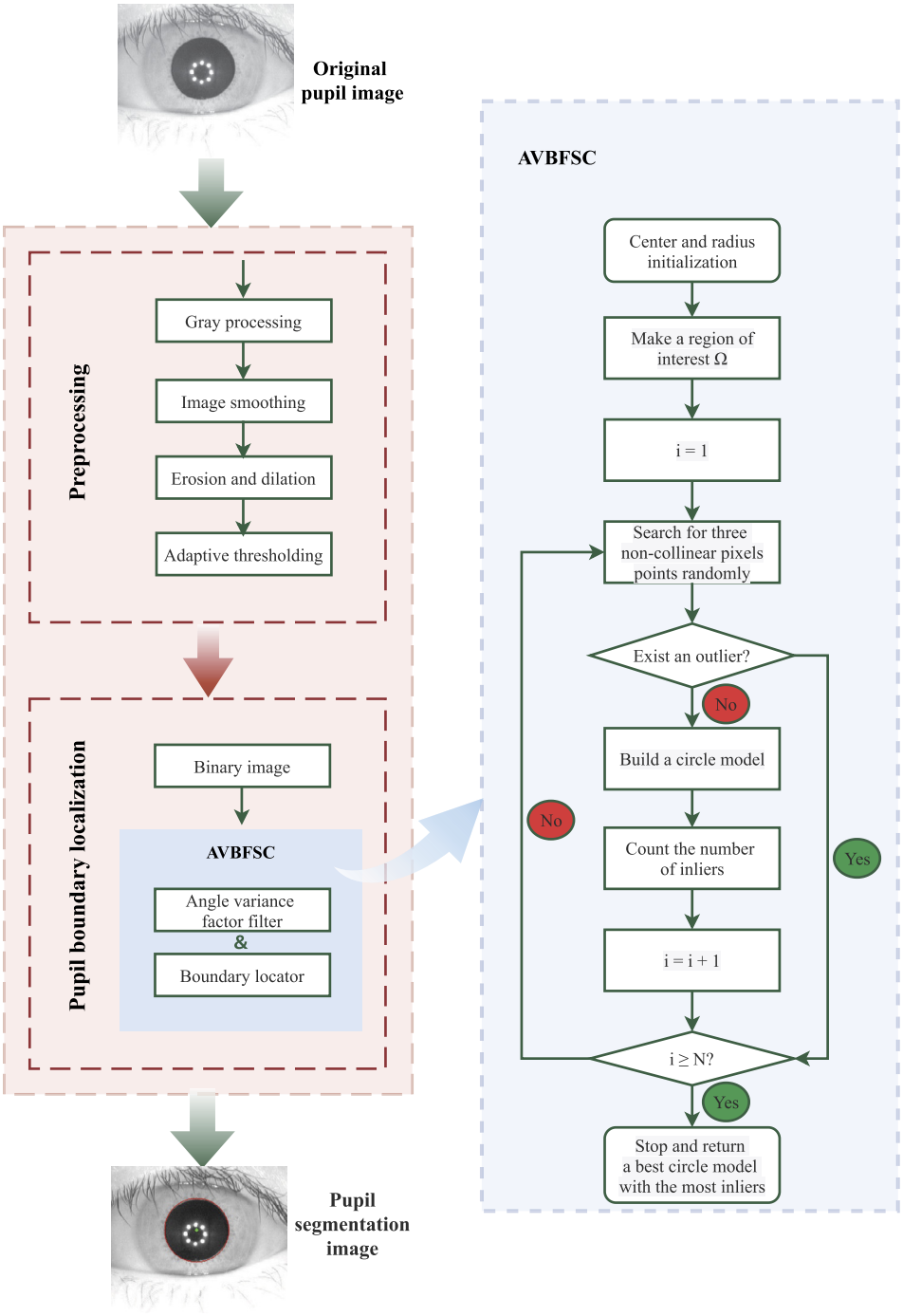

Fig. 1. Flowchart of pupil segmentation. The flowchart shows the overall steps of pupil segmentation, including image preprocessing and pupil boundary segmentation, in which the pupil boundary segmentation process is described in detail.

is proposed for better pupil segmentation without above perplexities, and it contains image preprocessing, pixel outliers filtering and circular mathematical modeling with the maximum number of inliers. The overall flowchart is as illustrated in Fig. 1. Experimental results on CASIA-Iris-V4-Interval dataset, CASIA-Iris-V4-Lamp dataset and Indian Institute of Technology Delhi (IITD) dataset indicate that our algorithm has achieved best precision and robust results under the condition of both ideal and specific non-ideal scenes. To summarize, we make the following contributions:

(1) We propose an outlier filter operator constructed by angle variance factor, which is able to eliminate the influence of outliers. Thus, our algorithm is more robust and adaptable to some specific non-ideal scenes including dark light conditions, eyelash occlusion, eyelid occlusion and off-gaze deflection.
(2) We propose a boundary locator and it learns a circular mathematical modeling by selecting sub-samples from pupil edge pixels randomly, which has a comparative segmentation result compared to state-of-the-art methods: convolution integro-differential operator (CIDO) [16], integer wavelet transform (IWT) [17] and Adaptive Threshold and Circular Hough Transform (ATCHT) [18].

The remainder of the paper is organized as follows: A description of previous work is introduced in Section 2. Our method for pupil segmentation including image preprocessing, angle variance

factor and sample consensus for training best circular mathematical modeling is presented in Section 3. Detailed comparative experiment results between our method and other state-of-the-art methods are provided in Section 4. In addition, we discuss the relationship between our work and some very related works in Section 5. In Section 6, we give a conclusion of our work and make a further research plan.

2. Related work

Pupil segmentation and iris recognition have attracted more researchers' attention, and a lot of work in this topic are completed. Here, we prepare a comprehensive introduction for these works in the fields of locating the inner and outer boundary of the iris.

Some researchers approximately regard pupil as a circle and propose some circular-edge based methods. Daugman [12] uses IDO and its variant, a circular-edge detector, to search for the circular path where there is maximum change in pixel values, by varying the radius 'r' and the center (x, y) of the circular contour. Radman et al. [19] make an initial approximation of the pupil center using the circular Gabor filter, and use IDO and CHT to find the iris and pupil boundaries. In addition, according to the scheme of coarse-to-fine as the same as Radman et al., Jan et al. [20] present a pupil boundary segmentation method including localizing a coarse pupil location in the eye image using the CHT and regularizing the pupillary boundary using a bi-valued adaptive threshold with 2D shape properties. For improving the robustness of pupil segmentation, Jan et al. [21] refine coarse pupil boundaries through the Fourier series. To relax the circular limits of pupil shape in the primary segmentation stage, Labati [22] proposes a method of polar spline for non-ideal iris image segmentation, in which the iris shape is approximated as a closed curve with arbitrary degrees of freedom, and to make a final refinement using CHT.

In addition, there are still some researchers who have made contributions to the field of pupil segmentation and iris recognition with different methods. Lee et al. [23] estimate the pupil center using orientation fields, followed by edge detection using a gradient. Then an approximate radius based on the circular histogram of the detected pupil edges is established. Unfortunately, the algorithm will work only if the entire iris is clearly visible in the image. Omran et al. [24] enhance the image by using histogram equalization and median filter to localize the pupil, then Gamma correction and blurring disk filter are used to determine the pupil boundary. However, the algorithm for removing eyelashes and eyelids should be modified, because the method used is subject to a significant error. In [25], a modified Wildes algorithm to solve the problem of pupil segmentation is proposed. In order to detect pupil edges, they create a method free from the issue of mirror points reflections, which consists of a morphological filter and a two-way scanning method. Then eyelids are detected using the Refine-Connect-Extend-Smooth (R-C-E-S). But authors do not test the algorithm for images recorded in visible light spectrum. Due to a variety of noise in the iris images, Hao et al. [26] use feature channel optimization to solve the problem of pupil segmentation. They use a coder-decoder based on Jensen-Shannon divergence to recalculate the weight of the feature channels, which enhances the useful information and suppresses the interference information in the noisy environments to boost the segmentation accuracy. In visible wavelength environments, there are many factors that affect the iris region which make the pupil segmentation more difficult and challenging. Thus, Sahmoud et al. [27] analyze the color information for different color spaces (RGB, YCbCr, and HSV) to select a suitable iris for further pupil segmentation process.

There exists a huge difference between our method and previous methods through reviewing the literature above. We have integrated an outlier filter into pupil segmentation process: we use an adaptive threshold different from previous global threshold to make image binarization, followed by a strong and powerful outlier filter and a robust boundary locator. The existing previous works haven't ever constructed explicitly an outlier detector when having a pupil segmentation yet, so it is just our outlier filter operator that makes it a reality to have a better pupil segmentation as well as a wide application range under different scenes in comparison with previous works. As a result, our method works well not only in ideal scenes but also in non-ideal scenes.

3. Methods

In this section, we make an introduction to our method. The main components are image preprocessing, the outlier filter and boundary locator, respectively. In image preprocessing, Bilateral filter is firstly used for removing noises and retaining pupil edge according to weighted coefficient c and s in formula (5). Next, to reduce the influence of infrared light and enhance the edge of pupil, erosion and dilation operations are used, and the side effects of eyelashes and infrared light are greatly weakened, while the pupil edge is enhanced, which is conducive to the segmentation of the pupil edge. Then, in order to highlight the edge of pupil, the image is binarized with adaptive threshold. Finally, our AVBFSC algorithm can filter the remaining outliers and give a best pupil equation from the last figure in Fig. 2.

3.1. Image preprocessing

Pupil images are color images with noises that have the adverse impact on the following pupil segmentation, and we need to remove noises before pupil segmentation. However, it is very unfriendly for pupil segmentation to remove image noises using Gaussian filter, owing to the disappearance of pupil edge after the use of Gaussian filter [28]. For removing noises and retaining pupil edge, we replace Gaussian filter with Bilateral filter [29,30]. Bilateral filter is composed of a low-pass domain filter and range filter. The low-pass domain filter is defined as follows:

$$h(x) = \kappa_d^{-1}(x) \int_{-\infty}^{\infty} \int_{-\infty}^{\infty} f(\xi)\, c(\xi, x)\, d\xi \tag{1}$$

$$\kappa_d(x) = \int_{-\infty}^{\infty} \int_{-\infty}^{\infty} c(\xi, x)\, d\xi \tag{2}$$

where $c(\xi, x)$ measures the geometric distance between the neighborhood center x and a nearby point ξ. Color images can be filtered out of high-frequency noise by using low-pass domain filter.

Range filter is defined in the same way:

$$h(x) = \kappa_r^{-1}(x) \int_{-\infty}^{\infty} \int_{-\infty}^{\infty} f(\xi)\, s(f(\xi), f(x))\, d\xi \tag{3}$$

$$\kappa_r(x) = \int_{-\infty}^{\infty} \int_{-\infty}^{\infty} s(f(\xi), f(x))\, d\xi \tag{4}$$

where $s(f(\xi), f(x))$ measures the photometric similarity between the pixel at the neighborhood center x and that of a nearby point ξ. Bilateral filtering is generally denoted by combining domain filter with range filter, as illustrated in the following formula:

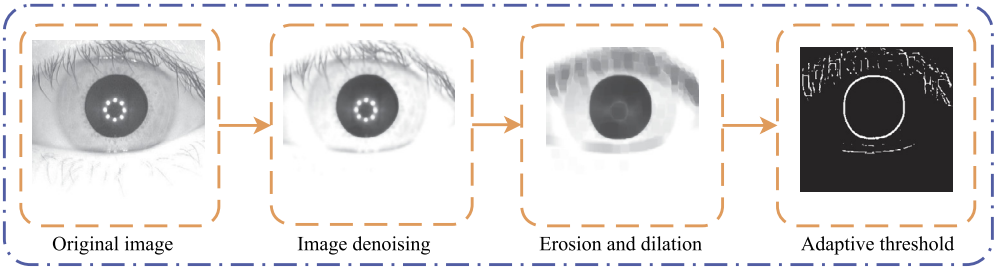

Fig. 2. Image preprocessing procedure. The procedure completes the task of processing the original image into a binary image.

$$h(x) = \kappa^{-1}(x) \int_{-\infty}^{\infty} \int_{-\infty}^{\infty} f(\xi)\, c(\xi, x) \cdot s(f(\xi), f(x))\, d\xi \tag{5}$$

with the normalization using following formula:

$$\kappa(x) = \int_{-\infty}^{\infty} \int_{-\infty}^{\infty} c(\xi, x)\, s(f(\xi), f(x))\, d\xi \tag{6}$$

where

$$c(\xi, x) = e^{-\frac{1}{2}(\frac{d(\xi, x)}{\sigma_d})^2}$$

and

$$s(\xi, x) = e^{-\frac{1}{2}(\frac{\delta(f(\xi), f(x))}{\sigma_r})^2}$$

For Bilateral filtering (formula (5)), the weighted coefficient of neighborhood filtering takes into account not only geometric distance (weighted coefficient c) but also gray similarity (weighted coefficient s). Intuitively, we can make a preliminary distinction between noises and normal points. If a noisy point appears in a smooth area, the difference between the point near the noise and its grayscale is about the same. Then the normal points in the neighborhood are assigned basically the same gray similarity weights because they are almost the same grayscale difference. Thus, filtering is approximate to gaussian mean filtering. However, for the edge details, the side with large difference in gray values (i.e. outside the boundary) is assigned smaller weight, while the weight inside the boundary is significant, which is exactly what the similarity function s can provide. Therefore, such an intuitive understanding can make it clear why Bilateral filtering can preserve boundary details. The denoising result of Bilateral filtering is the second figure in Fig. 2.

3.1.1. Erosion and dilation

To reduce the influence of infrared light and enhance the pupil edge, erosion and dilation operations are used. In erosion and dilation operations to grayscale image [31], the image and structuring element are represented by real-valued function $f(x, y)$ and $h(x, y)$, respectively. Grayscale erosion and dilation are respectively defined as follows:

$$(f \ominus h)(x, y) = inf_{(r,s)\in H}\{f(x+r, y+s) - h(r, s)\} \tag{7}$$

$$(f \oplus h)(x, y) = sup_{(r,s)\in H}\{f(x-r, y-s) + h(r, s)\} \tag{8}$$

where $(x, y) \in \mathbb{R}^2$, $H \subseteq \mathbb{R}^2$, $inf\{\}$ and $sup\{\}$ denote the infimum and supremum operators.

Erosion first eliminates the noises and shrinks the object, and then dilation expands the object again, noises have disappeared from the previous erosion. Now, it can be seen from the third figure of Fig. 2 that the side effects of eyelashes and infrared light are greatly weakened, while the pupil edge is strengthened, which makes the gray difference between the pupil and its neighbors become larger, which is conducive to the segmentation of the pupil edge.

3.1.2. Adaptive threshold

In order to highlight the position and edge of pupil, the image is binarized with adaptive threshold. Under the uneven lighting conditions, the difference of intensities between pupil pixels and other pixels are obvious, so we use adaptive threshold to obtain binary image. Concretely, the average intensity value of a 3×3 size pixel block around every pixel is chosen as a threshold to generate the binary image. The whole image preprocessing results are shown in Fig. 2.

3.2. Angle Variance based Filterable Sample Consensus: AVBFSC

The target pixel object that needed to be cared about displays on a binary image after above preprocessing (see the last figure in Fig. 2). This object contains not only the pupil edge pixels, but also outlier pixels such as eyelashes and eyelids. These outlier pixels have serious negative impacts on pupil segmentation without doubt, so it is essential to eliminate the negative impacts using our outlier filter constructed by angle variance factor.

3.2.1. Circular mathematical modeling description

To quantify the pupil edge, we model it with a circle. The formula of circular mathematical modeling is:

$$x^2 + y^2 - Dx - Ey - F = 0 \tag{9}$$

Since three non-collinear points can determine a circle, three non-collinear pixels on the pupil edge need to be found in order to calculate the parameters of the circular model. Assuming that (x_1, y_1), (x_2, y_2) and (x_3, y_3) are three arbitrary points on a circle. Let

$$P = \begin{pmatrix} x_2 - x_1 & y_2 - y_1 \\ x_3 - x_2 & y_3 - y_2 \end{pmatrix}$$

and

$$Q = \begin{pmatrix} x_2^2 - x_1^2 + y_2^2 - y_1^2 \\ x_3^2 - x_2^2 + y_3^2 - y_2^2 \end{pmatrix}$$

So here comes the estimation of circle's center $(\widehat{a}, \widehat{b})$ and radius $\widehat{r}$, respectively:

$$(\widehat{a}, \widehat{b}) = (\frac{D}{2}, \frac{E}{2}) = \frac{1}{2} P^{-1} Q \tag{10}$$

$$F = x_1^2 + y_1^2 - Dx_1 - Ey_1 \tag{11}$$

$$\widehat{r} = \sqrt{(\frac{D}{2})^2 + (\frac{E}{2})^2 + F} \tag{12}$$

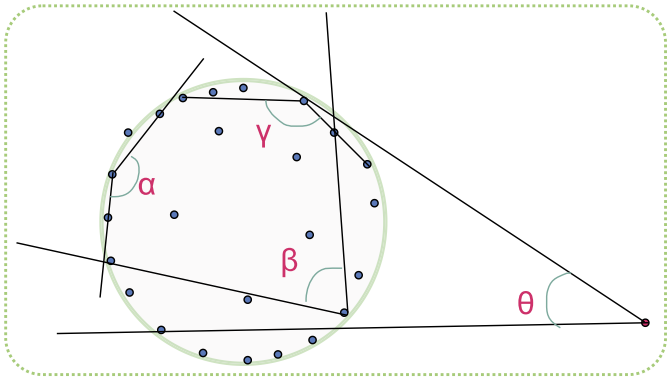

Fig. 3. A bio-mimetic pupil distribution schematic diagram with outliers, in which the red point is an outlier. (For interpretation of the colors in the figures, the reader is referred to the web version of this article.)

3.2.2. Angle variance factor (AVF)

When calculating the formula (10), formula (11) and formula (12), the optimal results are retained by randomly selecting subsamples from pupil edge pixels in the presence of small amounts of outliers. However, this way is able to eliminate the effect of the small amount of outliers, and a large number of outliers fundamentally make the estimation results largely deviate from the correct ones, so it leads to a failure pupil segmentation. Therefore, AVF is used to identify and filter a large number of outliers. In order to make a pupil segmentation accurately and robustly, we propose AVBFSC, in which eyelashes and eyelids are regarded as outliers and they need to be removed for minimizing negative effect in the task of pupil segmentation.

The common outlier detection methods mainly contain six types, such as clustering based [32], angle based [33], density based [34], high dimensional based [35–37], correlation based [38] and heteroscedasticity based [39]. We use AVF, an angle based outlier detection method, as a detection measure of outliers, and it is motivated by the intellectual intuition of geometric distribution of pixels (see Fig. 3). For a blue point within a cluster, the angles between the point to other points pairs differ widely, and it's the opposite for a red outside point of a cluster. As a result, AVF of the angles α, β and γ within a cluster has become larger than the angle θ outside a cluster. The AVF is defined formally:

Definition 1. Given a dataset $\mathcal{D} \subseteq \mathbb{R}^d$, a point $\overrightarrow{A} \in \mathcal{D}$, and a norm operator $\|\cdot\| : \mathbb{R}^d \longrightarrow \mathbb{R}_0^+$. The cross product is denoted by $\langle \cdot, \cdot \rangle : \mathbb{R}^d \times \mathbb{R}^d \longrightarrow \mathbb{R}$. For two points $\overrightarrow{B}, \overrightarrow{C} \in \mathcal{D}$, $\overrightarrow{BC}$ denotes the difference vector of $\overrightarrow{C} - \overrightarrow{B}$.

Note that three points $(\overrightarrow{A}, \overrightarrow{B}, \overrightarrow{C})$ are different but mutual. This means that $\overrightarrow{B} \in \mathcal{D} \setminus \{\overrightarrow{A}\}$, $\overrightarrow{C} \in \mathcal{D} \setminus \{\overrightarrow{A}, \overrightarrow{B}\}$ is the exact expression of $\overrightarrow{B} \in \mathcal{D}$, $\overrightarrow{C} \in \mathcal{D}$, respectively.

The Angle Variance Factor $AVF(\overrightarrow{A})$, shown in formula (13), is the variance over angles, weighted by the distance of the points, between the difference vector of $\overrightarrow{A}$ to all other pairs of in $\mathcal{D}$.

In order to detect outliers quantitatively, $LBAVF_\kappa(\overrightarrow{A})$, the lower bound of $AVF(\overrightarrow{A})$, is estimated conservatively to work as a minimum threshold for outliers detection (see formula (14)). For example, given a pixel θ and a threshold ϵ, if $\|AVF(\theta) - LBAVF_\kappa(\theta)\| \leq \epsilon$, the pixel θ is a noisy point.

$$AVF(\overrightarrow{A}) = VAR_{\overrightarrow{B},\overrightarrow{C} \in \mathcal{D}} \left(\frac{\left\langle \overrightarrow{AB}, \overrightarrow{AC} \right\rangle}{\left\| \overrightarrow{AB} \right\|^2 \cdot \left\| \overrightarrow{AC} \right\|^2} \right)$$

$$= \frac{\sum_{\overrightarrow{B} \in \mathcal{D}} \sum_{\overrightarrow{C} \in \mathcal{D}} \left(\frac{1}{\left\| \overrightarrow{AB} \right\| \cdot \left\| \overrightarrow{AC} \right\|} \cdot \frac{\left\langle \overrightarrow{AB}, \overrightarrow{AC} \right\rangle}{\left\| \overrightarrow{AB} \right\|^2 \cdot \left\| \overrightarrow{AC} \right\|^2} \right)^2}{\sum_{\overrightarrow{B} \in \mathcal{D}} \sum_{\overrightarrow{C} \in \mathcal{D}} \frac{1}{\left\| \overrightarrow{AB} \right\| \cdot \left\| \overrightarrow{AC} \right\|}} - \left(\frac{\sum_{\overrightarrow{B} \in \mathcal{D}} \sum_{\overrightarrow{C} \in \mathcal{D}} \frac{1}{\left\| \overrightarrow{AB} \right\| \cdot \left\| \overrightarrow{AC} \right\|} \cdot \frac{\left\langle \overrightarrow{AB}, \overrightarrow{AC} \right\rangle}{\left\| \overrightarrow{AB} \right\|^2 \cdot \left\| \overrightarrow{AC} \right\|^2}}{\sum_{\overrightarrow{B} \in \mathcal{D}} \sum_{\overrightarrow{C} \in \mathcal{D}} \frac{1}{\left\| \overrightarrow{AB} \right\| \cdot \left\| \overrightarrow{AC} \right\|}} \right)^2 \tag{13}$$

3.2.3. Our AVBFSC algorithm

We develop AVBFSC to accurately and stably calculate pupil center and radius for pupil boundary segmentation. The main steps of the algorithm are as follows:

STEP 1: The initial pupil center (O_x, O_y) and radius O_r are calculated by CHT from the binary image, and then a region of interest Ω is constructed, in which (O_x, O_y) is the center and $O_r \pm \delta \times O_r$ is the radius, and δ is an allowable tolerance coefficient.

STEP 2: Given the total number of sampling N, we randomly search for three non-collinear target pixels in region Ω, and use AVF to perform outlier detection among these three pixels.

STEP 3: If none of the three pixels are outliers, the center $(\widehat{a}_i, \widehat{b}_i)$ and radius $\widehat{r}_i$ of the circle are calculated. Then, we define a sample consensus set:

$$\chi_i^T = \left\{ (x_i, y_i) \in \Omega : \sqrt{(x_i - \widehat{a}_i)^2 + (y_i - \widehat{b}_i)^2} \leq \widehat{r}_i \right\}$$

and call (x_i, y_i) an inlier. Typically, the support of this circle is calculated by counting the number of inliers to the circle $N_{\chi_i^T} = \mu(\chi_i^T)$, and the circle with the most inliers is selected as the best estimation of pupil boundary. If at least one pixel point among the three pixels is the outlier, we stop the calculation of the circle for this time, and continue next calculation after going back to **STEP 2** until the number of sampling equals to N.

STEP 4: Return the center and radius of the best circle with the most inliers.

The detailed pseudocode for the AVBFSC algorithm is shown in Algorithm 1.

$$LBAVF_\kappa(\overrightarrow{A}) = \frac{\sum_{\overrightarrow{B} \in \mathcal{N}_\kappa(\overrightarrow{A})} \sum_{\overrightarrow{C} \in \mathcal{N}_\kappa(\overrightarrow{A})} \left(\frac{1}{\left\| \overrightarrow{AB} \right\| \cdot \left\| \overrightarrow{AC} \right\|} \cdot \frac{\left\langle \overrightarrow{AB}, \overrightarrow{AC} \right\rangle}{\left\| \overrightarrow{AB} \right\|^2 \cdot \left\| \overrightarrow{AC} \right\|^2} \right)^2}{\sum_{\overrightarrow{B} \in \mathcal{D}} \sum_{\overrightarrow{C} \in \mathcal{D}} \frac{1}{\left\| \overrightarrow{AB} \right\| \cdot \left\| \overrightarrow{AC} \right\|}} - \left(\frac{\sum_{\overrightarrow{B} \in \mathcal{N}_\kappa(\overrightarrow{A})} \sum_{\overrightarrow{C} \in \mathcal{N}_\kappa(\overrightarrow{A})} \frac{1}{\left\| \overrightarrow{AB} \right\| \cdot \left\| \overrightarrow{AC} \right\|} \cdot \frac{\left\langle \overrightarrow{AB}, \overrightarrow{AC} \right\rangle}{\left\| \overrightarrow{AB} \right\|^2 \cdot \left\| \overrightarrow{AC} \right\|^2} + R}{\sum_{\overrightarrow{B} \in \mathcal{D}} \sum_{\overrightarrow{C} \in \mathcal{D}} \frac{1}{\left\| \overrightarrow{AB} \right\| \cdot \left\| \overrightarrow{AC} \right\|}} \right)^2 \tag{14}$$

where R is the remainder term and the expression is:

$$R = \sum_{\overrightarrow{B} \in \mathcal{D}} \sum_{\overrightarrow{C} \in \mathcal{D}} \frac{1}{\left\| \overrightarrow{AB} \right\|^3 \cdot \left\| \overrightarrow{AC} \right\|^3} - \sum_{\overrightarrow{B} \in \mathcal{N}_\kappa(\overrightarrow{A})} \sum_{\overrightarrow{C} \in \mathcal{N}_\kappa(\overrightarrow{A})} \frac{1}{\left\| \overrightarrow{AB} \right\|^3 \cdot \left\| \overrightarrow{AC} \right\|^3} \tag{15}$$

where $\mathcal{N}_\kappa\left(\overrightarrow{A}\right) \subseteq \mathcal{D}$ denotes the field of set for the κ nearest neighbors of $\overrightarrow{A}$.

Algorithm 1: Angle Variance based Filterable Sample Consensus (AVBFSC).

Input: A binary pupil image $I(x, y)$, The number of search: N, Constant threshold: ϵ, Tolerance coefficient: δ.
Output: The best central coordinate and radius of pupil: $(\widehat{a}_{best}, \widehat{b}_{best})$ and $\widehat{r}_{best}$.

Give an initial center (O_x, O_y) and radius O_r using CHT on $I(x, y)$ and count the number of inliers n_0.
Construct a ring region with (O_x, O_y) as the center and $O_r \pm \delta \times O_r$ as the radius, denoted as Ω.
Initialization: $\widehat{a}_{best} = O_x$, $\widehat{b}_{best} = O_y$, $\widehat{r}_{best} = O_r$ and counter $i = 1$.
while $i \leq N$ **do**
  Search for three non-collinear target pixels arbitrarily from region Ω, indicated as $P_m (m = 1, 2, 3)$;
  if $\|AVF(P_m) - LBAVF_\kappa(P_m)\| \leq \epsilon$ **then**
    Go back and execute 4;
  else
    Calculate formula (10), formula (11) and formula (12) on P_m to obtain central coordinates, radius and the number of inliers: $(\widehat{a}_i, \widehat{b}_i)$, $\widehat{r}_i$ and n_i;
    if $n_i > n_{i-1}$ **then**
      $\widehat{a}_{best} = \widehat{a}_i$;
      $\widehat{b}_{best} = \widehat{b}_i$;
      $\widehat{r}_{best} = \widehat{r}_i$;
      $i = i + 1$;
    else
      Go back and execute 4;
return $\widehat{a}_{best}$, $\widehat{b}_{best}$ and $\widehat{r}_{best}$.

4. Experiments and results

The publicly available indoor non-ideal iris image datasets, CASIA-Iris-V4-Interval, CASIA-Iris-V4-Lamp and IITD, are used for our experiments. One can obtain them by visiting the website: http://biometrics.idealtest.org/findDownloadDbByMode.do?mode=Iris and https://web.comp.polyu.edu.hk/csajaykr/myhome/database_request/iris/. CASIA-Iris-V4-Interval dataset contains 2639 eye images of size 320 × 280 from 249 subjects, and each with approximately 1-10 images. CASIA-Iris-V4-Lamp dataset contains 16212 challenging eye images of size 640 × 480 from 411 subjects. IITD [40] contains total 1120 eyeimages collected from 224 individuals using the JIRIS, JPC1000, digital CMOS camera. This camera uses NIR illuminators while acquiring image data, and each image exhibits noise such as eyelashes, eyelids, eyebrows, contact lenses, focus and reflections. In the absence of ground truth of dataset used, we independently use an image annotation tool, namely, VGG Image Annotator (VIA) to make a manual pupil boundary labeling for 300 pupil images with circles by careful visual inspection (see Groundtruth in Fig. 5). Anyone can use VIA by logging in the website: https://gitlab.com/vgg/via. VIA can export the center and radius of pupil. It is called a nearly perfect pupil labeling when pupil boundaries coincide exactly with manual circumference i.e. a maximum deviation for pupil boundaries is less than 3 pixels in the experiment. On the contrary, it is incorrect pupil labeling when maximum deviation is more than 3 pixels. During manual labeling, the biggest challenge is that there is no way to avoid contrived errors in some degrees, so we try to make the labeled shape consistent with the real pupil shape as much as possible.

4.1. The precision of our proposed algorithm

AVBFSC is implemented on CASIA-Iris-V4-Interval, C-ASIA-Iris-V4-Lamp and IITD datasets through the software platform of Python version 3.6.6 on Intel Core i7 2.90 GHz processor with 8 GB RAM. Some segmentation samples are displayed in Fig. 4, where it is intuitively seen that our algorithm performs a good result.

It is indispensable to show the precision of AVBFSC to some extent using a greater accuracy (see Table 1). A lower FAR and a higher GAR are both important indicators to explain that this algorithm can overlap more pupil pixels and overlap less other pixels at the same time. The detailed components to define FAR and GAR are presented in the Fig. 5. True Positive (TP) represents that true pupil pixels can be recognized as pupil pixels correctly by using our algorithm. False Negative (FN) represents that true pupil pixels can be recognized as other pixels wrongly. False Positive (FP) represents that other pixels can be recognized as pupil pixels wrongly, and True Negative (TN) represents that other pixels can be recognized as other pixels correctly. So, the common performance metrics including Accuracy, FAR, GAR, Sensitivity, Specificity and Mean Intersection over Union (MIoU) are calculated respectively as:

$$Accuracy = \frac{TP + TN}{TP + FP + FN + TN} \times 100 \tag{16}$$

$$FAR = \frac{FP}{FP + TN} \times 100 \tag{17}$$

$$GAR = Sensitivity = \frac{TP}{TP + FN} \times 100 \tag{18}$$

$$Specificity = 1 - FAR = \frac{TN}{FP + TN} \times 100 \tag{19}$$

$$MIoU = \frac{TP}{FN + TP + FP} \times 100 \tag{20}$$

We implement three algorithms: CIDO [16], IWT [17] and ATCHT [18] and obtain six comparative evaluation results, as is illustrated in Table 1. These results indicate that our algorithm performs more precisely in comparison with the state-of-the-art methods, as is illustrated in Fig. 6.

4.2. The robustness of our proposed algorithm

Most pupil localization and segmentation methods have achieved pretty good results from ideal pupil image but have obtained bad results in the specific non-ideal scenes including dark light conditions, eyelash occlusion, eyelid occlusion and off-gaze deflection. Our algorithm has a strong outlier filtering capability to make a robust pupil segmentation ignoring the negative effect of above non-ideal scenes. We specially make a test on CASIA-Iris-V4-Lamp dataset and IITD dataset to highlight our algorithm's robustness, as are illustrated in Table 2 and Fig. 7, Table 3 and Fig. 8.

Since the normal distribution and homogeneity of variance of t-test don't meet, Mann-Withney-Wilcoxon test is performed to illustrate the significance of mean difference between our method and all comparisons (see Table 4). It's obvious that all the results are statistically significant. In addition, for demonstrating the superiority of our algorithm, the specific scenes selected from CASIA-Iris-V4-Lamp dataset are shown in Fig. 9. As be seen from Fig. 9, our algorithm performs very well but CIDO [16], IWT [17] and ATCHT [18] perform not pretty good, and in the four specific non-ideal scenes, their results are even obvious to deviate from the correct ones.

5. Discussion

In this section, we make a discussion about the relationship between our two main technologies for pupil segmentation. These two technologies are outlier detection and boundary segmentation, respectively.

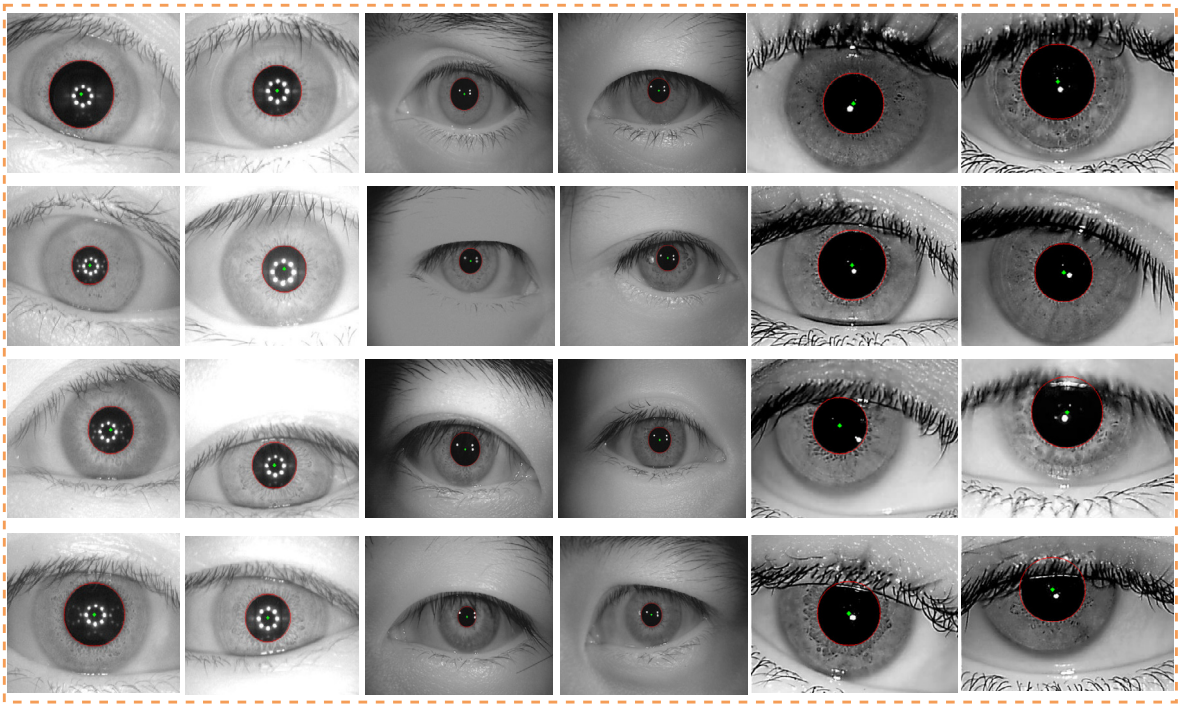

Fig. 4. Some segmentation results for CASIA-Iris-V4-Interval dataset (the first and second columns), CASIA-Iris-V4-Lamp dataset (the third and fourth columns) and IITD dataset (the fifth and sixth columns) after applying our proposed method.

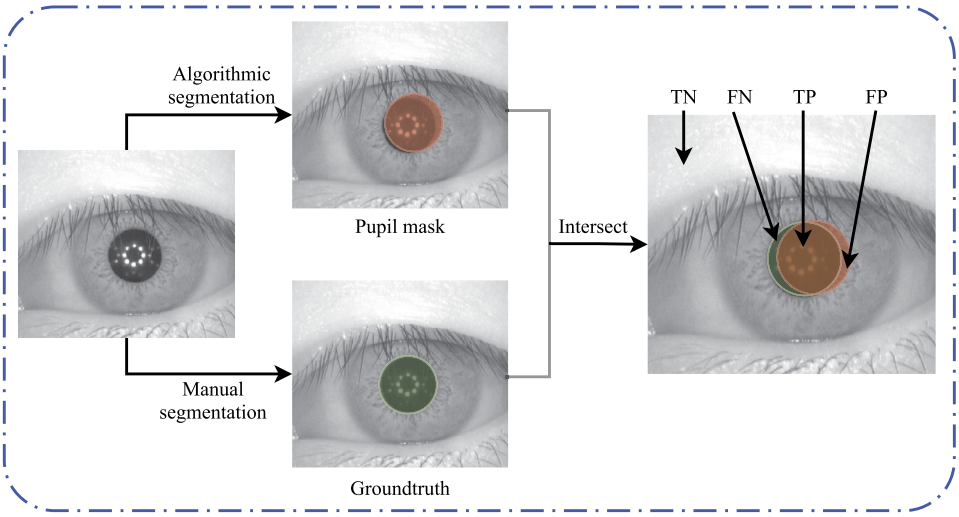

Fig. 5. Schematic diagram of indicator definition for pupil segmentation. Construction of TN, FN, TP and FP through the way of calculating overlapping area between manual segmentation and algorithmic segmentation.

Table 1
The comparative result of average accuracy, average run time for each image, FAR and GAR, in comparison with CIDO [16], IWT [17] and the state-of-the-art method: ATCHT [18], over 300 manually segmented images from CASIA-Iris-V4-Interval dataset. The number in brackets is standard deviation.

Methods	Accuracy (%)	Time (s)	FAR (%)	GAR *or* Sensitivity (%)	Specificity (%)	MIoU (%)
CIDO [16]	95.51(5.13)	1.53(0.32)	4.18(0.21)	95.16(5.09)	95.82(0.21)	95.54(0.16)
IWT [17]	97.46(4.62)	0.07(0.04)	3.69(0.12)	97.53(4.30)	96.31(0.12)	96.38(0.25)
ATCHT [18]	97.54(4.43)	**0.06(0.05)**	3.64(0.10)	97.55(3.13)	96.36(0.10)	96.88(0.22)
Ours	**98.99(2.98)**	0.55(0.03)	**2.09(0.11)**	**98.54(2.20)**	**97.91(0.11)**	**98.96(0.18)**

5.1. Outlier detection problem

In this subsection, we discuss the problem of outlier detection in pupil segmentation. Pixel outliers are ubiquitous in the images, and are also big obstacles for pupil segmentation or iris recognition. It is infrequent to research a specialized outlier detection approach for pupil segmentation in existing literature, but it is also certainly essential to remove the negative impact of outliers. We use AVF to detect outliers in the process of pupil segmentation according to the distribution of outliers so that

Table 2
The comparative result of average accuracy, average run time for each image, FAR and GAR over 300 manually segmented images from CASIA-Iris-V4-Lamp dataset. The number in brackets is standard deviation.

Methods	Accuracy (%)	Time (s)	FAR (%)	GAR *or* Sensitivity (%)	Specificity (%)	MIoU (%)
CIDO [16]	91.08(6.32)	2.98(0.36)	9.11(1.25)	90.34(5.98)	90.89(1.25)	91.24(2.83)
IWT [17]	92.47(5.96)	0.18(0.11)	8.09(1.23)	91.96(5.64)	91.91(1.23)	92.56(2.67)
ATCHT [18]	94.69(4.85)	**0.16(0.13)**	7.82(1.24)	92.33(4.93)	92.18(1.24)	93.59(2.48)
Ours	**95.72(4.22)**	1.58(0.12)	**5.12(1.07)**	**95.45(4.67)**	**94.88(1.07)**	**95.66(2.03)**

Table 3
The comparative result of average accuracy, average run time for each image, FAR and GAR over 200 manually segmented images from IITD dataset. The number in brackets is standard deviation.

Methods	Accuracy (%)	Time (s)	FAR (%)	GAR *or* Sensitivity (%)	Specificity (%)	MIoU (%)
CIDO [16]	88.06(6.02)	2.96(0.32)	10.14(2.35)	89.17(5.33)	89.86(2.35)	89.92(2.23)
IWT [17]	89.93(4.79)	0.20(0.17)	8.98(1.33)	90.59(5.59)	91.02(1.33)	90.76(2.39)
ATCHT [18]	92.66(4.80)	**0.16(0.16)**	7.98(1.34)	92.89(4.02)	92.02(1.34)	92.56(2.15)
Ours	**95.12(4.73)**	1.47(0.14)	**4.83(1.26)**	**95.86(4.05)**	**95.17(1.26)**	**95.98(1.96)**

Table 4
The statistical significance results for all comparisons using Mann-Withney-Wilcoxon test.

Comparisons	CASIA-Iris-V4-Interval		CASIA-Iris-V4-Lamp		IITD	
	P value	P significance	P value	P significance	P value	P significance
Ours vs CIDO [16]	≤ 0.001	***	≤ 0.001	***	≤ 0.001	***
Ours vs IWT [17]	0.029	*	≤ 0.001	***	≤ 0.001	***
Ours vs ATCHT [18]	0.033	*	0.042	*	0.007	**

* : $P \leq 0.05$.
** : $P \leq 0.01$.
*** : $P \leq 0.001$.

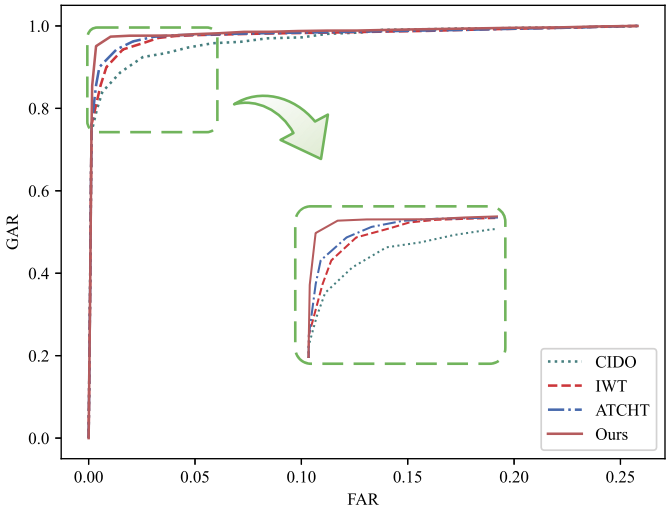

Fig. 6. Comparative ROC curve for different methods on CASIA-Iris-V4-Interval dataset. The ROC curve indicates that the performance of our proposed algorithm is best, the next is ATCHT [18], followed by IWT [17] and CIDO [16].

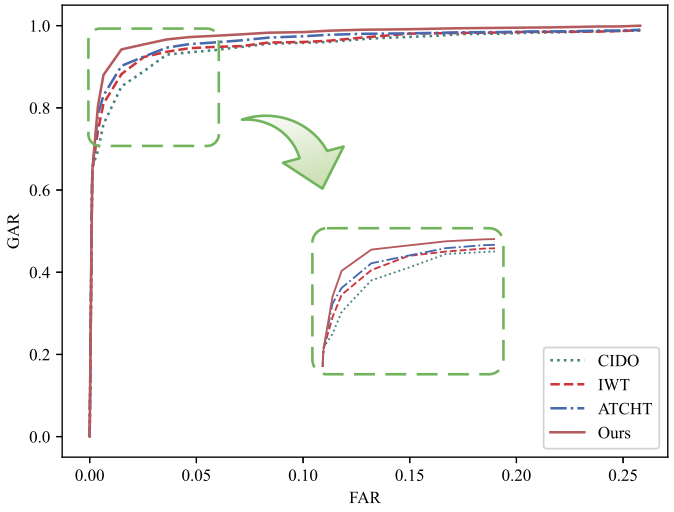

Fig. 7. Comparative ROC curve for different methods on CASIA-Iris-V4-Lamp dataset. The ROC curve indicates that the performance of our proposed algorithm is best and robust.

the following boundary segmentation process works more precisely.

5.2. Boundary segmentation problem

A circular mathematical modeling is constructed iteratively by calculating the formula (10), formula (11) and formula (12) using random selected three pixels from binary image. This way is also very effective under the condition of a small quantity of outliers and in the absence of AVF, but the circular mathematical modeling may have a substantial deviation from the correct one caused by a large quantity of outliers. So this boundary locator embedded with AVF for filtering out most of outliers is so powerful to get a best circular model with most inliers for pupil segmentation. To summarize, AVF and this training way of circle make an important contribution to our precise and robust algorithm.

5.3. Computational complexity analysis

The computational complexity of our method is quantified by using scan times of an image. The size of iris image is $n \times p$ in our dataset. The initialization of center and radius using CHT can cost $n \times p$, and detection of outliers in a ring region Ω costs $0.2n \times p$, and computational complexity of circle computing is determined by total sampling times N, and it is equal to $(150 \times 0.2 = 30)n \times p$ when $N = 150$ in our algorithm. Thus, it costs a total of $(1 + 30 = 31)$ scans in our algorithm when achieves scanning one image.

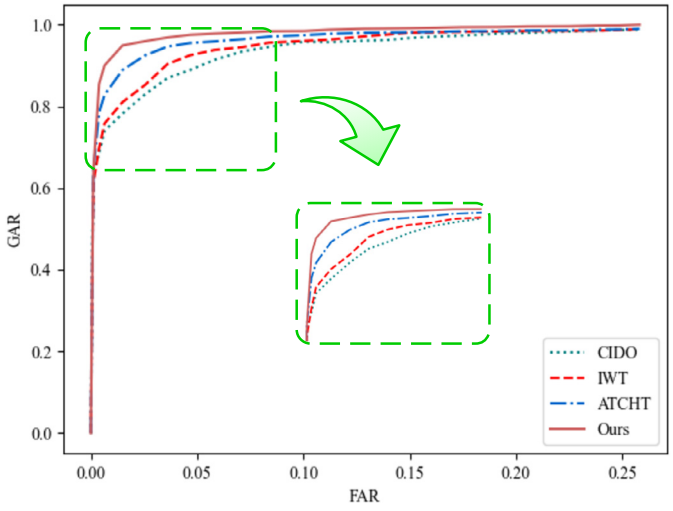

Fig. 8. Comparative ROC curve for different methods on IITD dataset. The ROC curve indicates that the performance of our proposed algorithm is best and robust.

For CIDO, the operator searches for the circular path where there is maximum change in pixel values, by varying the radius 'r' and the center (x, y) of the circular contour. The operator is applied iteratively with the amount of smoothing progressively reduced in order to obtain accurate localization. The variables x, y and r belong to the ranges [0; n], [0; p] and [0; R] respectively, and this method has the computational complexity of $R \times n \times p$, i.e. R scans. Pupil radius is about 1/4 of the length of short side of the image, so CIDO has the computational complexity of $1/4 \times 280 = 70$ scans. IWT has the computational complexity of $n \times p \times log(np) = 4$ scans, because it is derived from wavelet transform. ATCHT is adopted to localize pupil boundaries with the help of CHT, Rubber Sheet Model (RSM) and Contrast-Limited Adaptive Histogram Equalization (CLAHE). RSM is used in normalization stage to eliminate upper eyelashes and eyelid. CLAHE is adopted to overcome the low contrast problem of pupil image. Thus, ATCHT has the computational complexity of $(1 + 1 + 1 = 3)$ scans.

6. Conclusion

In total work of this paper, we propose AVBFSC to filter out outliers of pixels and make a pupil boundary segmentation using circular mathematical modeling. Results on CASIA-Iris-V4-Interval dataset and CASIA-Iris-V4-Lamp dataset show the superiority of our algorithm for non-ideal iris images in terms of accuracy and robustness. Our method is able to make a pupil segmentation accuracy of 98.99%, 95.72% and 95.12% on CASIA-Iris-V4-Interval dataset, CASIA-Iris-V4-Lamp dataset and IITD dataset on iris images captured indoors under near-infrared environment. However, Our technique relies heavily on the results of image preprocessing. When there is no pupil contour or few pixels in the contour after preprocessing, our method can not iteratively calculate the best pupil equation. In addition, since the random search strategy of our method consumes a certain amount of time, it cannot be implemented in real time or produce economic benefits in enterprises. We are going to improve applicability on iris images captured in the more demanding environment in further research.

CRediT authorship contribution statement

Jitao Zhong: Conceptualization, Formal analysis, Methodology, Software, Writing – original draft. **Dixin Wang:** Data curation, Validation. **Hongtong Wu:** Software. **Peng Wang:** Visualization. **Minqiang Yang:** Investigation. **Hong Peng:** Supervision, Writing – review & editing. **Bin Hu:** Project administration, Supervision, Writing – review & editing.

Declaration of competing interest

The authors declare that they have no known competing financial interests or personal relationships that could have appeared to influence the work reported in this paper.

Acknowledgments

The authors are thankful to the Chinese Academy of Science's Institute of Automation (CASIA) and Indian Institute of Technology Delhi (IITD) who granted the research community free access to their respective iris databases. This work was supported in part by the National Key Research and Development Program of China (Grant No. 2019-YFA0706200), in part by the National Natural Science Foundation of China (Grant No. 61632014, No. 61627808, No. 618-02159), in part by the Fundamental Research Funds for the Central Universities (No. lzujbky-2021-kb06).

References

[1] Haocong Rao, Shihao Xu, Xiping Hu, Jun Cheng, Bin Hu, Augmented skeleton based contrastive action learning with momentum lstm for unsupervised action recognition, Inf. Sci. 569 (2021) 90–109.
[2] Shihao Xu, Haocong Rao, Hong Peng, Xin Jiang, Yi Guo, Xiping Hu, Bin Hu, Attention based multi-level co-occurrence graph convolutional lstm for 3d action recognition, IEEE Int. Things J. (2020) 1.
[3] Haocong Rao, Siqi Wang, Xiping Hu, Mingkui Tan, Yi Guo, Jun Cheng, Bin Hu, Xinwang Liu, A self-supervised gait encoding approach with locality-awareness for 3d skeleton based person re-identification, IEEE Trans. Pattern Anal. Mach. Intell. (2021).
[4] M. Karnan, Akila Muthuramalingam, Krishnaraj Nagappan, Biometric personal authentication using keystroke dynamics: a review, Appl. Soft Comput. 11 (2011) 1565–1573.
[5] Dan Hansen, Qiang Ji, In the eye of the beholder: a survey of models for eyes and gaze, IEEE Trans. Pattern Anal. Mach. Intell. 32 (2010) 478–500.
[6] Yingzi Du, Chein-I. Chang, 3d combinational curves for accuracy and performance analysis of positive biometrics identification, Opt. Lasers Eng. 46 (2008) 477–490.
[7] Fan Yang, Qilu Wu, Xiping Hu, Jiancong Ye, Yuting Yang, Haocong Rao, Rong Ma, Bin Hu, Internet of things enabled data fusion method for sleep healthcare applications, IEEE Int. Things J. (2021) 1.
[8] Kevin Bowyer, Karen Hollingsworth, Patrick Flynn, Image understanding for iris biometrics: a survey, Comput. Vis. Image Underst. 110 (2008) 281–307.
[9] Arun Ross, Iris recognition: the path forward, IEEE Comput. Soc. 43 (2010) 30–35.
[10] Craig Belcher, Yingzi Du, Region-based sift approach to iris recognition, Opt. Lasers Eng. 47 (2009) 139–147.
[11] Wei-Long Zheng, Bo-Nan Dong, Bao-Liang Lu, Multimodal emotion recognition using eeg and eye tracking data, in: 2014 36th Annual International Conference of the IEEE Engineering in Medicine and Biology Society, EMBC 2014, vol. 2014, 2014, pp. 5040–5043.
[12] P.P. Chitte, M.E. In, J.G. Rana, S. Taware, Advanced security system using rfid and iris recognition system using ica, pca, Daugman's rubber sheet model together, Int. J. Comput. Appl. 48 (13) (2012).
[13] Mousumi Sardar, Sushmita Mitra, B. Uma Shankar, Iris localization using rough entropy and csa: a soft computing approach, Appl. Soft Comput. 67 (2018) 61–69.
[14] R.P. Wildes, Iris recognition: an emerging biometric technology, Proc. IEEE 85 (9) (1997) 1348–1363.
[15] Andreas Uhl, Peter Wild, Weighted adaptive hough and ellipsopolar transforms for real-time iris segmentation, in: Proceedings - 2012 5th IAPR International Conference on Biometrics, ICB 2012, 2012.
[16] S. Buterin, Uniform stability of the inverse spectral problem for a convolution integro-differential operator, Appl. Math. Comput. 390 (2021) 125592.
[17] Z.N. Al-Kateeb, S.J. Mohammed, Encrypting an audio file based on integer wavelet transform and hand geometry, TELKOMNIKA Indones. J. Electr. Eng. 18 (4) (2020) 2012–2017.
[18] Jwad Ali Ridha, Jamila Harbi Saud, Iris segmentation approach based on adaptive threshold value and circular hough transform, in: 2020 International Conference on Computer Science and Software Engineering (CSASE), 2020, pp. 32–37.
[19] Abduljalil Radman, Kasmiran Jumari, Nasharuddin Zainal, Iris segmentation in visible wavelength environment, Proc. Eng. 41 (2012).

Fig. 9. Some specific comparative segmentation results of four different algorithms in four non-ideal scenes from CASIA-Iris-V4-Lamp dataset. The row denotes four specific non-ideal scenes: dark light, eyelid occlusion, eyelash occlusion and off-gaze deflection, respectively; The column denotes four different algorithms: CIDO [16], IWT [17], the state-of-the-art method: ATCHT [18] and our proposed algorithm, respectively.

[20] Farmanullah Jan, Imran Usman, Shahrukh Agha, Reliable iris localization using hough transform, histogram-bisection, and eccentricity, Signal Process. 93 (2013) 230–241.
[21] F. Jan, N. Min-Allah, S. Agha, I. Usman, I. Khan, A robust iris localization scheme for the iris recognition, Multimed. Tools Appl. 80 (3) (2021) 1–27.
[22] Ruggero Labati, Enrique Muñoz, Vincenzo Piuri, Arun Ross, Fabio Scotti, Non-ideal iris segmentation using polar spline ransac and illumination compensation, Comput. Vis. Image Underst. 188 (2019).
[23] S. Lee, D. Lee, Y. Park, Pupil segmentation using orientation fields, radial non-maximal suppression and elliptic approximation, Adv. Electr. Comput. Eng. 19 (2) (2019) 69–74.
[24] Maryim Omran, Ebtesam N. AlShemmary, An iris recognition system using deep convolutional neural network, J. Phys. Conf. Ser. 1530 (1) (2020) 012159.
[25] Ilke Simsek, Can Şirolu, Analysis of surgical outcome after upper eyelid surgery by computer vision algorithm using face and facial landmark detection, Graefe Arch. Clin. Exp. Ophthalmol. 259 (2021) 3119–3125.
[26] Kangli Hao, Guorui Feng, Yanli Ren, Xinpeng Zhang, Iris segmentation using feature channel optimization for noisy environments, Cogn. Comput. 12 (2020) 1–12.
[27] Shaaban Sahmoud, Hala N. Fathee, Fast iris segmentation algorithm for visible wavelength images based on multi-color space, in: Advanced Concepts for Intelligent Vision Systems, Springer International Publishing, Cham, 2020, pp. 239–250.
[28] S. Hu, D.A. Hall, F. Zubler, R. Sznitman, W. Wimmer, Bayesian brain in tinnitus: computational modeling of three perceptual phenomena using a modified hierarchical gaussian filter, Hear. Res. 410 (5) (2021) 108338.
[29] Xiaosong Li, Fuqiang Zhou, Haishu Tan, Wanning Zhang, Congyang Zhao, Multimodal medical image fusion based on joint bilateral filter and local gradient energy, Inf. Sci. 569 (2021) 302–325.
[30] S. Paris, F. Durand, A fast approximation of the bilateral filter using a signal processing approach, Int. J. Comput. Vis. 81 (1) (2009) 24–52.
[31] L. Zhao, J. Wang, Y. Li, Colour morphological operators based on formal concept analysis, Signal Image Video Process. 14 (1) (2019) 151–158.
[32] M. Li, R. Kashef, A. Ibrahim, Multi-level clustering-based outlier's detection (mcod) using self-organizing maps, Big Data Cogn. Comput. 4 (4) (2020).
[33] Ninh Pham, Rasmus Pagh, A near-linear time approximation algorithm for angle-based outlier detection in high-dimensional data, in: Proceedings of the 18th ACM SIGKDD International Conference on Knowledge Discovery and Data Mining, KDD '12, Association for Computing Machinery, New York, NY, USA, 2012, pp. 877–885.
[34] Shenfei Pei, Feiping Nie, Rong Wang, Xuelong Li, An efficient density-based clustering algorithm for face groping, Neurocomputing 462 (2021) 331–343.
[35] Tao Wang, Qun Li, Bin Chen, Zhonghua Li, Multiple outliers detection in sparse high-dimensional regression, J. Stat. Comput. Simul. 88 (1) (2018) 89–107.
[36] Tao Wang, Zhonghua Li, Outlier detection in high-dimensional regression model, Commun. Stat., Theory Methods 46 (14) (2017) 6947–6958.
[37] Junlong Zhao, Chao Liu, Lu Niu, Chenlei Leng, Multiple influential point detection in high dimensional regression spaces, J. R. Stat. Soc., Ser. B, Stat. Methodol. 81 (2) (2019) 385–408.
[38] Junlong Zhao, Chenlei Leng, Lexin Li, Hansheng Wang, High-dimensional influence measure, Ann. Stat. 41 (5) (2013) 2639–2667.
[39] Chun Gun Park, Inyoung Kim, Outlier detection using difference-based variance estimators in multiple regression, Commun. Stat., Theory Methods 47 (24) (2018) 5986–6001.
[40] Ajay Kumar, Arun Passi, Comparison and combination of iris matchers for reliable personal authentication, Pattern Recognit. 43 (3) (2010) 1016–1026.

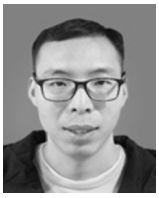

Jitao Zhong is a Ph.D. candidate at the Gansu Provincial Key Laboratory of Wearable Computing, School of Information Science and Engineering, Lanzhou University. He received his master's degree from School of Mathematics & Statistics, Lanzhou University. He is interested in research fields about affective computing, multimodal fusion and image processing.

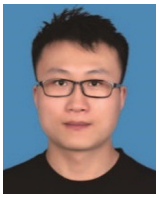

Dixin Wang is currently pursuing the M.E. degree at the Gansu Provincial Key Laboratory of Wearable Computing, School of Information Science and Engineering, Lanzhou University, Lanzhou, China. He received the B.E. degree from the School of Information Engineering, North University of China, Taiyuan, China, in 2019. His research interests include biomedical signal processing and deep learning.

Hongtong Wu is currently pursuing the M.E. degree at the Gansu Provincial Key Laboratory of Wearable Computing, School of Information Science and Engineering, Lanzhou University, Lanzhou, China. He received the B.E. degree from the School of Computer and Communication Engineering, Northeastern University at Qinhuangdao, Qinhuangdao, China, in 2020. His research interests include affective computing, biomedical signal processing and pattern recognition.

Peng Wang is a Ph.D. candidate at School of Mathematics & Statistics, Huazhong University of Science and Technology. He received his master's degree from School of Mathematics & Statistics, Lanzhou University. His current research interest is deep learning, biomedical signal processing and image processing.

Minqiang Yang received his Ph.D. degree in computer science from Lanzhou University. He is an engineer at the Gansu Provincial Key Laboratory of Wearable Computing, School of Information Science and Engineering, Lanzhou University. His current research interests include affective computing, image processing, machine learning, and automatic depression detection.

Hong Peng (Member, IEEE) received the Ph.D. degree from Lanzhou University, Lanzhou, China. From 2010 to 2011, he was as a Visiting Scholar with the Institute of Computer System, ETH Zurich, Switzerland. He is currently a Professor with the School of Information Science and Engineering, Lanzhou University. He is in charge of several projects from National Natural Science Foundation of China, Central College Foundation Project of Lanzhou University and Youth Cross-Project of Lanzhou University. He has authored or co-authored over 30 papers in peer-reviewed journals, conferences, and book chapters. He is involved in the work of biosensors, biological signal processing, and emotional characteristics analysis. His research areas include bioinformation processing and ubiquitous affective computing.

Bin Hu (Senior Member, IEEE) is currently a Professor and the former Dean of the School of Information Science and Engineering, Lanzhou University, Lanzhou, China, and an Adjunct Professor with the Computing Department, The Open University, Milton Keynes, U.K. His research areas focus on affective computing, pervasive computing, and computational behavior modeling.

Dr. Hu was an elected Fellow of the Institution of Engineering and Technology (IET). He was a recipient of many research awards, including the 2014 China Overseas Innovation Talent Award, the 2016 Chinese Ministry of Education Technology Invention Award, the 2018 Chinese National Technology Invention Award, and the 2019 WIPO-CNIPA Award for Chinese Outstanding Patented Invention. He is the TC Co-Chair of computational psychophysiology and cognitive computing in the IEEE Systems, Man, and Cybernetics (SMC) Society and the Vice-Chair of the TC 9.1. Economic, Business, and Financial Systems on Social Media at the International Federation of Automatic Control (IFAC). He is also a Member-at-Large of the Association for Computing Machinery (ACM) China Council and the Vice-Chair of the China Committee of the International Society for Social Neuroscience. He serves as the Editor-in-Chief for IEEE Transactions on Computational Social Systems and an Associate Editor for IEEE Transactions on Affective Computing.